UCSF

UC San Francisco Previously Published Works

Title

Discrete microstructural cues for the attenuation of fibrosis following myocardial infarction.

Permalink

https://escholarship.org/uc/item/00f8x69c

Journal

Biomaterials, 35(31)

ISSN

0142-9612

Authors

Pinney, James R
Du, Kim T
Ayala, Perla
<u>et al.</u>

Publication Date

2014-10-01

DOI

10.1016/j.biomaterials.2014.07.005

Peer reviewed

Discrete Microstructural Cues for the Attenuation of Fibrosis Following Myocardial Infarction

James R. Pinney[1,2], **Kim Du**[3], **Perla Ayala**[1,4], **Qizhi Fang**[3], **Rich Sievers**[3], **Patrick Chew**[5], **Lawrence Delrosario**[6], **Randall J. Lee**[1,3], and **Tejal A. Desai**[1,5,*]

[1]UC Berkeley – UCSF Graduate Group in Bioengineering, 1700 4th Street, QB3 Byers Hall Room 203, San Francisco, CA, 94158

[2]UCSF Medical Scientist Training Program, 1700 4th Street, QB3 Byers Hall Room 203, San Francisco, CA, 94158

[3]UCSF Department of Medicine, Cardiovascular Research Institute and Eli and Edythe Broad Center of Regeneration Medicine and Stem Cell Research, Box 1354, 513 Parnassus Ave, MS Room 1136, San Francisco, CA, 94143

[4]Beth Israel Deaconess Medical Center, Department of Surgery, Center for Life Science Surgery/ BIDMC – 11th Floor, 3 Blackfan Circle, Boston, MA, 02115

[5]UCSF Bioengineering and Therapeutic Sciences, 1700 4th Street, Room 203, QB3 Box 2520, San Francisco, CA, 94158

[6]UCSF School of Medicine, 513 Parnassus Ave, MS Room 1136, San Francisco, CA, 94143

Abstract

Chronic fibrosis caused by acute myocardial infarction (MI) leads to increased morbidity and mortality due to cardiac dysfunction. We have developed a therapeutic materials strategy that aims to mitigate myocardial fibrosis by utilizing injectable polymeric microstructures to mechanically alter the microenvironment. Polymeric microstructures were fabricated using photolithographic techniques and studied in a three-dimensional culture model of the fibrotic environment and by direct injection into the infarct zone of adult rats. Here, we show dose-dependent down-regulation of expression of genes associated with the mechanical fibrotic response in the presence of microstructures. Injection of this microstructured material into the infarct zone decreased levels of collagen and TGF-β, increased elastin deposition and vascularization in the infarcted region, and improved functional outcomes after six weeks. Our results demonstrate the efficacy of these

*Corresponding Author: Tejal A. Desai, PhD, 1700 4th Street, Room 203, QB3 Box 2520, San Francisco, CA, 94158. Phone: 415-514-9695. Fax: 415-476-2414. tejal.desai@ucsf.edu.

discrete anti-fibrotic microstructures and suggest a potential therapeutic materials approach for combatting pathologic fibrosis.

Keywords

Polyethylene Glycol Dimethacrylate; Cardiac Tissue Engineering; Photolithography; Fibrosis; ECM; Collagen

Introduction

Coronary heart disease is a daunting challenge in the United States with nearly one million new or recurrent MIs each year [1]. Although strategies for the acute management of an MI have proven to be effective at improving mortality and morbidity outcomes, the development of fibrous scar tissue in the infarct zone often leads to challenging chronic complications and functional insufficiencies [2]. These subsequent morbidities highlight the importance of the cardiac microenvironment in the development of pathology following MI as stiffening and thinning of the infarcted wall leads to diminished pumping efficiency with further progression to heart failure [3–8].

Recent work has focused on developing therapies to reintegrate healthy muscle tissue or stem cell sources into the infarcted heart to induce regeneration of the damaged muscle [9–12]. Others have demonstrated the advantage of mechanically supportive bulk injectable gels composed of processed biological materials to improve functional outcomes after MI [13–17]. Despite the early successes of some of these strategies, the dense fibrotic tissue that begins to arise within days of the MI presents a barrier to both the biologic and mechanical mechanisms of these potential therapies [18]. Cell survival or invasion into the scar tissue is met with resistance from the pathologically altered microenvironment that is hostile to cellular integration [19]. Meanwhile, stiffening of the muscle tissue with subsequent decrease in contractile function limits the positive mechanical influence of bulk material injections [15]. Therapies that directly target fibrosis at the local level after an infarct could alleviate the maladaptive mechanical reaction responsible for the chronic decline in heart function.

In addition to laying down the extracellular matrix (ECM) that creates the physiologic mechanical environment in the heart, cardiac fibroblasts have been shown to play a critical role in the injury response and limited regenerative potential of heart muscle [3–8,20,21]. After MI, a population of highly contractile myofibroblasts develops in the wake of inflammatory matrix metalloproteinases, which degrade the injured muscle. Transformation initiated by increased local tensile stresses on resident fibroblasts that are no longer able to offload mechanical stress by attachment to a robust network of ECM proteins may contribute to this pathologic response, resulting in accelerated ECM production and increased release of signaling factors [7,8,20,22,23].

We have previously utilized a system of polymeric microstructures, termed "microrods" and "microcubes" that act as anchors for cell traction and demonstrated their effects on fibroblast growth in 2D and 3D culture [24–28]. Using basic techniques in photolithography, this

system allows us to tune the shape and mechanical stiffness of these microstructures to enhance interactivity and efficacy in mitigating myofibroblastic transformation. This platform is also highly versatile and can be studied both *in vitro* and *in vivo* to assess the mechanistic interactions and therapeutic potential of polymeric microstructures. Here we demonstrate the effects that micromechanical environmental cues have on cells and tissues by elucidating changes in the regulation of fibrotic activation at the transcriptional level and correlating this to demonstrated therapeutic efficacy of microstructure injections into infarcted myocardium.

Materials and Methods

Microstructure fabrication

Microrods (100 μm × 15 μm × 15 μm) and microcubes (15 μm × 15 μm × 15 μm) were fabricated from PEG-DMA as previously described using commercially available materials [24] and re-suspended in complete media for *in vitro* studies or sterile saline solution for intra-cardiac injections (Figure 1). Briefly, polyethylene glycol dimethacrylate (PEG-DMA) (MN = 750, Sigma Aldrich, St. Louis, MO) was diluted with Calcium and Magnesium-free 1× Phosphate Buffered Saline (PBS). The photo-initiator 2,2-dimethoxy-2-phenylacetophenone (DMPA) (Sigma Aldrich, St. Louis, MO) solubilized at 100 mg/mL in 1-vinyl-2-pyrrolidinone (Sigma Aldrich, St. Louis, MO) was then added to this mixture in equal volume to the PBS added and vortexed thoroughly. The solution was spun to a 15μm thick layer on a piranha-solution-cleaned silicon wafer (Addison Engineering, San Jose, CA) and exposed through a photomask to a 405 nm UV light source using a Karl Suss MJB3 mask aligner (Suss Microtec, Garching, Germany) to crosslink the desired regions in the shape of microrods (100 μm × 15 μm × 15 μm) or microcubes (15 μm × 15 μm × 15 μm). Microstructures were rinsed, scraped from the surface gently using a cell scraper, and sterilized in 70% ethanol. Before use, microstructures were centrifuged to allow aspiration of the ethanol and re-suspension at the desired number-density in saline solution.

Cell culture and qPCR

Murine 3T3 fibroblasts (ATCC, Manassas, VA) were harvested between passages 18 and 20 and mixed with either microrods at a high ratio (1:1) or a low ratio (1:5) of structures to cells, or microcubes at a high ratio (20:3) or low ratio (4:3) and added to liquid state Growth Factor Reduced, High Concentration Matrigel (Lot 42155) (BD Biosciences, San Jose, CA) doped with 10% (v/v%) of a 0.2% gelatin solution (Sigma Aldrich, St. Louis, MO) to a final protein concentration of 4 mg/mL. The mixture was then seeded into ~2 mm thick cultures in a 96-well plate before gelling at 37 °C. After gelation, fresh media was added on top and replaced every other day for four days. Genetic material was harvested by standard TRIzol (Life Technologies, Carlsbad, CA) extraction protocols.

A Viia7 qPCR machine (Life Technologies, Carlsbad, CA) was used to measure relative expression levels of gene targets as compared to housekeeping gene 60s ribosomal protein L19 (rpL19). Expression levels of genes for mmp2, SRF, YAP, and TAZ were evaluated using Fast SYBR Green Mastermix (Life Technologies, Grand Island, NY) and custom

made DNA primers (Integrated DNA Technologies, Coralville, IA) in triplicate for three biological replicates (See Supplementary Table 1).

Infarct model and microstructure delivery

The animal protocol for induction of MI was approved by the Committee for Animal Research of the University of California San Francisco and was performed in accordance with the recommendations of the American Association for Accreditation of Laboratory Animal Care. The ischemia-reperfusion model used in this study has been extensively tested in our lab. All injections were performed successfully and there were no complications resulting from surgery or injection in any animal. Protocols were approved by the IACUC of UCSF. All studies were performed in two rounds of experiments (Experimental Group 1: Saline – n = 10, Microrod – n = 20, Microcubes – n = 9, Experimental Group 2: Saline – n = 8, Microrod – n = 11, Microcube – n = 11).

To produce the MI model, female Sprague-Dawley rats (180–220g) underwent occlusion of the left anterior descending coronary artery for 30 minutes followed by reperfusion while under general anesthesia achieved by inhalation of 2% L/min isoflurane. The chest was then closed and the animal was allowed to recover. The rats were randomized two days after MI to saline-injected, microrod-injected, or microcube-injected treatment groups, and were given one intramuscular injection into the heart wall under blinded conditions via ultrasound guided transthoracic injection using a 29-gauge syringe. Each injection consisted of 50 μL of sterile 0.9% sodium chloride solution (APP Pharmaceuticals, LLC, Schaumburg, IL) containing no microstructures (n = 18), 2.5×10^5 microrods (n = 31), or 1.65×10^6 microcubes (n = 20) and was delivered to the center of the infarct region as visualized by hyperechoic signal on ultrasound. Successful injection was confirmed by local increase in ultrasound signal in the vicinity of the syringe.

Echocardiography

Transthoracic echocardiography was performed with a 15-MHz linear array transducer system (Sequoia c256, Acuson, Erlangen, Germany) on all animals under 2% L/min isoflurane. Echocardiography was done prior to injection on day two post-MI and six weeks post-injection using standard methods that have been performed reproducibly in our lab [29,30]. To determine the ejection fraction at 48 hours and six weeks, the ventricular shadow was outlined in both systole and diastole and the single plane area length algorithmic method was applied. Two-dimensional images were obtained in both parasternal long- and short-axis views at the papillary muscle level. With sufficient two-dimensional image slips, M-mode images were also obtained and the wall thickness and LV internal dimensions (LVD) were measured according to the leading edge method of the American Society of Echocardiography. End diastolic volume (EDV), end systolic volume (ESV), and ejection fraction (EF) were calculated by the machine software algorithm from the parasternal long axis view using the single plane area length method. Transverse images were obtained at three levels: basal (at the tip of the mitral valve leaflets), middle (at the papillary muscle level), and apical (distal to papillary muscle but before the cap of the cavity). All image analyses were performed in a blinded fashion. In cases where the ventricular shadow was

not clearly identifiable in the 48 hour or six week image, the heart in question was excluded from echocardiographic analyses.

Histology

Sacrifice was performed after six weeks by maintaining the animal at 5% L/min isoflurane for five minutes, followed by bilateral thoracotomy and injection of potassium chloride into the right atrium to arrest the heart in diastole. The heart was then extracted and frozen in OCT (Sakura Finetech USA, Inc., Torrance, CA) on 2-methylbutane (Sigma Aldrich, St. Louis, MO) on dry ice and sectioned for histology and image analysis. Tissue blocks were cryo-sectioned at a thickness of 10 μm starting at the apex of the left ventricle and collecting 10 serial sections every 350 μm until 100 sections were collected. Sections were stained by standard protocol with aniline blue (Sigma Aldrich, St. Louis, MO) or fixed in 100% acetone for 10 minutes, blocked with 10% BSA (for TGF-β, Myosin Heavy Chain, and Actin sections) and dual endogenous enzyme block (DAKO, Carpinteria, CA) (for Elastin, αSMA, and Cardiac Troponin sections), followed by incubation with primary and secondary antibodies using standard protocols. In brief, samples were incubated overnight with primary antibodies at 4°C in a solution of 0.5% Triton X-100 and 1% BSA in PBS (Elastin, ab21610, 1:250, Abcam, Cambridge, England), (αSMA, a2547, 1:400, Sigma Aldrich, St. Louis, MO), (Cardiac Troponin, ab47003, 1:400, Abcam, Cambridge, England), (TGF-β, sc-146, 1:250, Santa Cruz Biotechnology, Inc., Dallas, TX), (Myosin Heavy Chain, sc-20641, 1:200, Santa Cruz Biotechnology, Inc., Dallas, TX). After rinsing, secondary antibody was added (Goat anti-mouse IgG HRP conjugated, ab6789, 1:500, Abcam, Cambridge England), (Goat anti-rabbit IgG HRP conjugated, ab6721, 1:500, Abcam, Cambridge England), (Goat anti-rabbit alexafluor 488, a11008, 1:200, Life Technologies, Carlsbad, CA) for 45 minutes at room temperature. For fluorescent staining, DAPI (1:1000) and rhodamine phalloidin (1:200) were added as a counterstain (Life Technologies, Carlsbad, CA). For HRP-conjugated secondaries, diaminobenzidine (DAKO, Carpinteria, CA) was added to one section and timed for each antibody until the tissue turned sufficiently colored and was repeated for all sections stained with that antibody. Adjacent sections were treated with secondary antibody without primary antibody to assess the extent of non-specific staining for each secondary antibody.

Image Analysis

Images were taken using a Nikon 6D optical microscope (NIKON Instruments, Inc., Melville, NY) at 4–20× magnification and quantified for staining metrics using Adobe Photoshop (Mountain View, CA). All image acquisition and analysis was performed in a blinded fashion. Rubrics of histological exclusion were pre-determined for each type of staining to address damaged sections. For blinded analysis of elastin and α-SMA staining, at least three sections separated by 350 μm, each, had to include both an identifiable ventricular cavity as well as a clearly outlined infarct zone. For blinded analysis of fluorescent TGF-β staining, a sequential pair of undamaged, serially sectioned slices was required for appropriate background signal subtraction. These analyses were performed on the Experimental Group 2 subset of animals from the entire group consisting of n = 8 saline-treated, n = 11 microrod-treated, and n = 11 microcube-treated animals. Any histological

section from this sub-group that did not meet these minimum analytic rubrics was excluded from histological analysis in a blinded fashion.

For collagen analysis, five sections of each heart were selected from throughout the coronal plane of the infarct zone and stained with Aniline Blue simultaneously to assess the distribution and density of collagen in the injured hearts. After isolating the blue channel of the left ventricle from color images of these sections taken at 4× magnification, a colorimetric heat map was applied, transforming the blue color density of each pixel to a linear green-red spectrum with pure red representing maximum staining intensity and pure green representing the absence of staining. Sections with an identifiable population of microstructures still embedded in the tissue were then assessed for local collagen staining density by applying a color threshold to all pixels at a consistent color value (chosen at pure yellow) and randomly selecting circular regions of 125 μm diameter throughout the infarct zone. The highlighted microstructures were then overlaid on this image and the percentage of thresholded pixels per circular area (subtracting pixels occupied by microstructures) as compared to the percent of pixels occupied by microstructures was plotted for 75 sampled regions.

Antibody staining for elastin in the tissue sections was quantified by averaging the ratio of the area of elastin staining in the infarct zone to the area of the infarct in multiple coronal sections and normalizing this averaged ratio across all three groups. A similar analysis was performed for quantification of fluorescently labeled TGF-β in the infarct region using background subtraction of adjacent negative control stained sections without the use of primary antibody.

Cryo-sectioned and fixed tissue slices were also evaluated for vascularization density in the infarct region six weeks after infarct. Tissues were stained with αSMA and vessels were counted. To be included in the count, vessel structures were required to fulfill the following criteria: 1) be contained entirely within the scarred region (as determined by overlay of a sequential Aniline Blue-stained section); 2) be identified by positive αSMA signal in a continuous circle or ellipse; and 3) fall in the appropriate range of diameters greater than 10 μm and less than 100 μm. All imaging analyses were done in a blinded fashion.

Statistical Analysis

All values for continuous variables are listed as the mean ± 95% confidence intervals, unless otherwise indicated. *In vitro* analysis was performed using a two-tailed Student's t-test. *In vivo* markers were assessed for normality (See Supplementary Figure 1) before using a one-tailed (paired or unpaired) student's t-test to detect expected improvements in fibrotic response and functional performance as instructed by the anti-fibrotic results of the *in vitro* experiments and previous work [24,25]. In cases where there were signs of possible left or right-skew of the data, a one-tailed Mann-Whitney test was used as an alternative consideration of significance. Adjustments for small sample size were not deemed necessary due to the continuous distribution of all data sets and the close concordance with a normal distribution. Statistical significance was set at $p < 0.05$. Correlations were determined using a Pearson Correlation Coefficient assuming a linear relationship. Analysis was performed with Microsoft Excel.

Results

In vitro model of fibroblast-microstructure interactions

We evaluated the effect of the presence of polymer microrods and microcubes on fibroblasts grown in a soft three-dimensional construct of Matrigel. Microrods (100 μm × 15 μm × 15 μm) and microcubes (15 μm × 15 μm × 15 μm) were fabricated at a stiffness of at least 20 kPa, as this stiffness was shown to be the threshold for maximum biological effect in previously published work by our group (Figure 2A,B) [24]. These shapes were chosen to evaluate the effect of two extremes of contact area and aspect ratio on cell-microstructure interaction. Fibroblasts cultured in the presence of these polymer microstructures are highly interactive with the introduced physical cues. Whereas fibroblasts tend to cluster on or near microrod structures, they demonstrate a more dynamic interaction with microcubes by extending cell processes to bind to or envelop the structure (Figure 2C,D). In contrast, fibroblasts grown in the absence of microstructures showed a much more characteristic growth pattern with multiple long cell processes and increased spreading area (Figure 2E).

Incorporation of two dose concentrations of microstructures were compared to cultures in gels not containing microstructures to assess transcription-level changes in fibroblasts interacting with stiff extracellular cues in a soft gel environment. To examine the effect of these microstructures on the TGF-β pathway, which is crucial to the fibrotic response to injury and myofibroblastic transformation [31,32], we analyzed the levels of SRF and mmp2, both of which are indicated in regulation and activity of TGF-β (Figure 3A,B) [33–35]. Although low concentrations of microrods and microcubes had little effect on transcription of these two factors, increased concentration of microstructures resulted in a nearly two-fold decrease in expression levels of mmp2 and SRF in response to microrods (p=0.007 and 0.01, respectively) and a consistent trend of down-regulation in response to microcubes.

Upstream sensing of mechanical stimuli encountered by the cells in the three-dimensional constructs was examined by measuring expression levels of known mechanotransductive mediators, YAP and TAZ (Figure 3C,D) [36–38]. Expression of YAP followed a parallel trend with low concentrations of microstructures having no significant effect while a high concentration of microrods elicited a significant down-regulation (0.71×, p = 0.02) and high concentration microcubes exhibited a similar, yet non-significant trend (0.75×, p = 0.2). Expression of TAZ, on the other hand, was significantly decreased in the presence of high concentration microrods (0.58×, p = 0.04), low concentration microcubes (0.77×, p = 0.03), and high concentration microcubes (0.74×, p = 0.004).

Microstructure influence on the infarcted cardiac microenvironment

Both microrods and microcubes were delivered into the infarct zone by ultrasound-guided, transthoracic injection 48 hours after the induction of an infarct. After six weeks, the hearts were harvested and fresh frozen for subsequent cryo-sectioning and immunohistochemical analysis. This allowed us to examine tissue-level effects of polymeric microstructures on infarcted tissue as compared to saline-injected hearts.

Aniline blue staining delineates the scarred region and allows identification of injected microstructures, as seen in false color in Figure 4A. Evaluating the prevalence of collagen staining in proximity to injected microstructures shows a significant inverse relationship between microstructure location and collagen density with a Pearson Correlation Coefficient of R = 0.71 (Figure 4B). Integration of microstructures with cardiac tissue at the cellular level, as opposed to space displacement seen in many types of bulk material injections, was confirmed histologically, showing the presence of cells throughout deposits of injected microstructures (Figure 4C).

Evaluation of elastin staining reveals a two-fold increase in relative elastin content in the infarct zone of microrod-treated hearts (normalized mean = 2.09, range = 0.61 – 3.04) as compared to saline-treated hearts (normalized mean = 1.0, range = 0.47 – 1.95) (p = 0.01, student's t-test; p = 0.05, Mann-Whitney test), with a mild, non-significant increase in microcube-treated hearts (normalized mean = 1.31, range = 0.33 – 2.84) (p = 0.2, student's t-test; p = 0.4, Mann-Whitney test) (Figure 5A).

Fluorescent staining for TGF-β with background subtraction using adjacent negative control stained sections also revealed reproducible trends between the three groups. Figure 5C shows a representative infarct from a saline-treated heart stained for TGF-β with dense and pervasive staining throughout the infarct zone, as is expected in the inflammatory, fibrotic environment. Reduced infarct-bound TGF-β staining was noted in microrod-treated (mean = 27%, range = 15 – 39%) and microcube-treated (mean = 30%, range = 5 – 53%) hearts, as quantified in Figure 5B and represented in Figure 5D. TGF-β staining in the microrod-treated hearts was nearly one-half of that in saline-treated hearts (mean = 43%, range = 23 – 64%) (p = 0.01), while microcube-treated hearts showed approximately two-thirds as much TGF-β, on average (p = 0.05) (Figure 5B).

False-color highlighting of vessel structures that meet these criteria is shown for representative saline-treated (Figure 6A) and microcube-treated (Figure 6B) heart sections. Quantification of independent vessel structures in all three groups yielded a significant relationship of nearly two-fold increase in vascularization in both types of microstructure-treated hearts (microrods: mean = 28.3 vessels/mm^2, range = 19.3 – 54.9, p = 0.01, student's t-test; p = 0.005, Mann-Whitney test; microcubes: mean = 30.7 vessels/mm^2, range = 21.3 – 52.4, p = 0.005, student's t-test; p = 0.002, Mann-Whitney test, as compared to saline-treated hearts: mean = 18.4 vessels/mm^2, range = 12.7 – 24.3) (Figure 6C).

Functional benefits of intra-cardiac microstructure injection after MI

To assess the cardiac function of the infarcted hearts, the percent change in ejection fraction (EF) was evaluated over a six week period. Ligation of the LAD followed by reperfusion resulted in a precipitous decline in cardiac function in this standard rodent infarct model [29]. Over six weeks, the function of the heart continued to deteriorate, as seen in the saline-injected group, which demonstrated an 11.9% comparative loss in EF over the course of the experiment (mean = −11.9%, range = −48.3% – 10.4%). The injection of microrods or microcubes directly into the infarct zone 48 hours after infarct, however, mitigated this loss of cardiac function (Figure 7a). Microrod-treated hearts showed only a 2.7% comparative loss in EF (mean = −2.7%, range = −32.3% – 59.8%, p = 0.08), whereas microcube-treated

hearts showed a significant average relative increase in EF of 1.4% after six weeks (mean = 1.4%, range = −33.0% – 37.2%, p = 0.03). Internal one-tailed paired t-test comparison within each group corroborates a non-significant absolute change in EF from two days to six weeks in both the microrod (p = 0.08) and microcube-treated (p = 0.5) groups, while the saline-treated group experienced a significant 6% absolute drop in EF (p = 0.008), demonstrating the improved maintenance of cardiac function in the chronic setting.

Although the same dose of microrods or microcubes was delivered to each infarct, the delivery efficiency varied depending on infarct geometry and injection kinetics. To assess the efficiency of each injection, microstructures were stained and counted in five sections throughout the depth of the infarct. Microcubes were recovered in the tissue at a ratio roughly equal to the larger number of microcubes injected as compared to microrods to achieve control of total volume of polymer injected. A direct linear correlation was found between the number of microstructures recovered histologically and the change in EF over six weeks (Figure 7b). This correlation describes a significant relationship between dose and functional response of the microstructure-based therapy with a Pearson Correlation Coefficient of R = 0.66. When greater than 200 microstructures (microrods or microcubes) were counted across five distinct sections of the infarct region, ten of eleven animals had a change in EF that was better than the average for the saline-injected group and nine of eleven animals showed absolute improvement in their EF as compared to post-infarct measurements.

Histological examination of a heart with a highly efficient delivery of microstructures demonstrates marked effects both at the tissue level and the functional level (Figure 7c). The region of the infarct proximal to the microstructure injection shows decreased collagen content as compared to the distal infarct region. Illustratively, the animal with the highest number of microstructures recovered across five sections (700) showed the greatest improvement in EF over six weeks (+50%).

Discussion

Existing therapies to treat chronic complications of MI have been largely hampered by the robust fibrotic response of the injured tissue [39–41]. Differentiation and long-term over-proliferation of the myofibroblast subpopulation of stromal cells leads to the development of dense scar tissue and thinning of the ventricular muscle wall, which presents a physical barrier to both exogenous and limited endogenous regeneration mechanisms [39–41]. After rapid development of the scarred tissue, strategies to introduce progenitor cell populations or induce re-muscularization of the injured region face tremendous obstacles in the form of the hostile microenvironment of the post-infarct zone [15,19]. We have utilized a physiologic stiffness-relevant three-dimensional tissue assay to mimic the early infarct zone microenvironment and study the mechanisms through which microtopographical features exert their anti-fibrotic effects. Here, we demonstrate this minimally invasive materials-based strategy that uses discrete micro-environmental cues to influence and attenuate the development of fibrotic scar tissue after MI.

Studies examining cellular interaction with substrates and constructs in which they are grown have highlighted the importance of the microenvironment in dictating cellular behavior and response to both physiologic and pathologic stimuli [15,24,27,28,30,42–45]. In particular, we focused on mediators of the mechanotransductive pathways responsible for translating environmental cues into behavioral responses at the cellular level.

Recent work has indicated the role of YAP/TAZ transcriptional regulation in responding to matrix elasticity to effect subsequent downstream changes in cell behavior and growth characteristics through direct signal transduction to the nucleus [36–38]. In two-dimensional growth environments, YAP and TAZ expression levels have been shown to be decreased on softer substrates when cellular tension is low and stress fiber formation is reduced as compared to stiff substrates [36]. In three dimensions, however, decreased matrix elasticity leads to reactive stiffening of fibroblastic cells in the matrix, as illustrated by the cardiac injury response. This may be due to the limited availability of binding sites in the sparse ECM, which leads to increased deposition of ECM proteins and contraction of the environment to regenerate appropriate tension levels, as seen, for example, in the wake of MI. In this setting, we hypothesize that YAP/TAZ transcription would be heightened in fibroblasts exposed to a soft three-dimensional matrix that leads to the development of increased cell processes and cellular tension (See Figure 2). Replacing the "missing" ligands in the three-dimensional milieu with rigid microstructures may serve to anchor fibroblasts and facilitate the generation of appropriate cellular tension. This attenuates YAP/TAZ production that is pathologically triggered by the increased cellular tension created by far-reaching, contractile fibroblastic cell processes.

The dose-dependent decrease of YAP and TAZ transcription in response to the introduction of both microrods and microcubes in a soft three-dimensional environment suggests that the presence of exogenous micro-environmental cues can deactivate mechanotransductive pathways that lead to fibroblastic activation, and may further lead to modulation of activation of the TGF-β pathway at large, as indicated by the concomitant changes observed in mmp2 and SRF. SRF is known to up-regulate and translocate to the nucleus when cells experience high tension. Similarly, mmp2 is up-regulated in response to the increased transcription of TGF-β, along with increased release of latent matrix-bound TGF-β [31–33,38]. The decrease in mmp2 in response to decreased SRF could be an example of a valuable check on the positive feedback cycle normally generated in injured tissue as transcribed and released metalloproteinases continue to cleave the surrounding ECM and release further latent TGF-β stores, resulting in self-perpetuation of the overactive fibroblastic response.

This concerted effect may be critical to the therapeutic potential of exogenously introduced microtopographical cues, as was demonstrated by our animal studies. Endogenously, activation of pathways that lead to increased transcription and nuclear translocation of factors such as YAP, TAZ, and SRF may ultimately lead to the production and deposition of stiff ECM collagen and fibronectin proteins in response to elevated levels of TGF-β [6,35]. Following infarct, inflammatory components lead to the destruction of the native ECM with reactive myofibroblastic transformation as increased TGF-β release triggers fibroblasts to over-produce stiff collagen to repair injured tissue. Attenuating this runaway response

through manipulation of the microenvironment may lead to a reduction in pathologic production of stiff collagen and highly cross-linked ECM components. In turn, this compliant tissue may facilitate improved penetration by vascular beds and functional muscle tissue, leading to more rapid and effective recovery

Previously, our lab has shown that microstructural cues can lead to decreased proliferation and production of ECM proteins by fibroblasts in three-dimensional culture which, from this current work, can be speculated to derive from decreased activation of stress-induced mechanotransductive pathways [24,25]. This is corroborated by the contrasting decrease in local collagen deposition in injured MI tissue in the vicinity of injected microstructures and the increased deposition of softer ECM components, such as elastin. We propose that introducing artificial anchors for cells to bind to in the softened, post-infarct matrix reduces mechanotransduction-instigated up-regulation of TGF-β release and collagen deposition, and, instead, favors deposition of softer ECM components that are more physiologically relevant to a healthy, uninjured microenvironment. Ultimately, this may be responsible for creating an injured environment that can passively coordinate with healthy myocardial contraction.

Recent research into other materials strategies for bolstering cardiac recovery after infarct has utilized bulking agents to artificially increase wall thickness in the infarcted zone in order to decrease wall tension [13,16,17,30,44]. Although the introduction of microstructures into the cardiac muscle tissue inherently supplies a small amount of bulking agent (~1 μL/injection), it seems more likely that the mechanism of action is independent of this relatively insignificant volume addition. The small size of the discrete structures enables them to travel in all directions between tissue planes and spread distal to the injection site, leading to increased global tissue impact area with minimal local volume effects. Instead, it may be attributed to the high surface area presented by the injected microstructures that allows widespread distribution and interaction with large fibroblastic populations throughout the infarcted region. This, in turn, decreases local cellular tension throughout the damaged tissue, mitigating the reactive fibrotic response.

Although our *in vitro* work suggested that the higher aspect ratio microrods enjoyed greater efficacy, possibly attributed to their increased hydrodynamic profile and thus heightened effective resistance to cellular contractile forces, our *in vivo* results indicate that the total surface area available for cell adhesion may be the critical factor in predicting therapeutic potential of microstructural shape. This helps to explain the apparent increased therapeutic efficacy of the low profile microcubes over high aspect ratio microrods, as the total polymer volume-controlled injection of microcubes yielded 40% more surface area for cell interaction. In addition, this may indicate why some histologic metrics showed greater improvement in the microrod group due to the focal nature of the discontinuous thin-section analysis. These effects may not have been as dispersed throughout the entire infarct zone to impart as great a functional benefit in the microrod case due to the reduced surface area of contact presented by the comparatively lower number of injected microrods versus microcubes. The shape profile of the microcube group may have also facilitated increased injection efficiency, tissue dispersion, and, ultimately, improved therapeutic outcomes. Future studies will utilize methods to improve delivery efficiency through the syringe and to

control for surface area availability of different structure shapes to better understand the role of microstructure geometry in affecting fibroblastic development in infarcted tissue.

It is important to recognize that although there is a strong correlation between microstructure delivery efficiency to the heart muscle and functional outcomes, as well as significant parallel trends in vascularity and TGF-β expression in the infarct zone in microstructure-treated groups, the complete list of causative phenomena are likely multifaceted and complex, and this study is not situated to draw complete conclusions about their nature. Continued experiments using non-cardiac models of tissue fibrosis are underway to help elucidate the important effectual parameters of this promising anti-fibrotic material strategy while limiting some of the challenges of intra-cardiac study. This could further elucidate the mechanisms by which micro-structured materials can be used as a viable therapeutic strategy for fibrotic pathologies.

Conclusion

We have demonstrated the use of discrete mechanical cues to alter pathways of mechanotransductive activation in a three-dimensional microenvironment and their potential as an effective anti-fibrotic therapy in the setting of acute MI. Introduction of a small volume of polymeric microstructures to the injured heart was shown to decrease local collagen density and TGF-β activation, increase elastin and vascular density, and, ultimately, mitigate chronic functional losses caused by the runaway myofibroblastic response in the post-infarct heart. In addition, we are currently examining the long-term release of therapeutic molecules from the hydrogel matrix of the microstructures to concomitantly recruit regenerative cell populations or reduce local inflammation over long periods in the vicinity of the injected material, broadening the full potential of this multifunctional therapeutic strategy. This strategy presents a cost-effective and minimally invasive materials approach to combat complications of pathologic scar tissue and could be used in concert with other therapeutics to attenuate the pervasive chronic complications of myocardial fibrosis and pave the way for more effective recovery from MI.

Supplementary Material

Refer to Web version on PubMed Central for supplementary material.

Acknowledgments

References

1. Go AS, Mozaffarian D, Roger VL, Benjamin EJ, Berry JD, Borden WB, et al. Heart disease and stroke statistics--2013 update: a report from the American Heart Association. Circulation. 2013; 127:e6–e245. [PubMed: 23239837]

2. Wilson P, Douglas P, Alpert JS, Simons M, Breall JA. Prognosis after myocardial infarction. UpToDate. Last updated 2013. Available from URL: http://www.uptodate.com/contents/prognosis-after-myocardial-infarction.

3. Camelliti P, Borg TK, Kohl P. Structural and functional characterisation of cardiac fibroblasts. Cardiovasc Res. 2005; 65:40–51. [PubMed: 15621032]

4. Sun Y. Myocardial repair/remodelling following infarction: roles of local factors. Cardiovasc Res. 2009; 81:482–490. [PubMed: 19050008]

5. Brown RD, Ambler SK, Mitchell MD, Long CS. The cardiac fibroblast: therapeutic target in myocardial remodeling and failure. Annu Rev Pharmacol Toxicol. 2005; 45:657–687. [PubMed: 15822192]

6. Creemers EE, Pinto YM. Molecular mechanisms that control interstitial fibrosis in the pressure-overloaded heart. Cardiovasc Res. 2011; 89:265–272. [PubMed: 20880837]

7. Hinz B. Formation and function of the myofibroblast during tissue repair. J Invest Dermatol. 2007; 127:526–537. [PubMed: 17299435]

8. Hinz B. The myofibroblast: paradigm for a mechanically active cell. J Biomech. 2010; 43:146–155. [PubMed: 19800625]

9. Beltrami AP, Barlucchi L, Torella D, Baker M, Limana F, Chimenti S, et al. Adult cardiac stem cells are multipotent and support myocardial regeneration. Cell. 2003; 114:763–776. [PubMed: 14505575]

10. Ieda M, Fu J-D, Delgado-Olguin P, Vedantham V, Hayashi Y, Bruneau BG, et al. Direct reprogramming of fibroblasts into functional cardiomyocytes by defined factors. Cell. 2010; 142:375–386. [PubMed: 20691899]

11. Johnston PV, Sasano T, Mills K, Evers R, Lee S-T, Smith RR, et al. Engraftment, differentiation, and functional benefits of autologous cardiosphere-derived cells in porcine ischemic cardiomyopathy. Circulation. 2009; 120:1075–1083. [PubMed: 19738142]

12. Chugh AR, Beache GM, Loughran JH, Mewton N, Elmore JB, Kajstura J, et al. Administration of cardiac stem cells in patients with ischemic cardiomyopathy: the SCIPIO trial: surgical aspects and interim analysis of myocardial function and viability by magnetic resonance. Circulation. 2012; 126:S54–S64. [PubMed: 22965994]

13. Plotkin M, Vaibavi SR, Rufaihah AJ, Nithya V, Wang J, Shachaf Y, et al. The effect of matrix stiffness of injectable hydrogels on the preservation of cardiac function after a heart attack. Biomaterials. 2014; 35:1429–1438. [PubMed: 24268664]

14. Kichula ET, Wang H, Dorsey SM, Szczesny SE, Elliott DM, Burdick JA, et al. Experimental and computational investigation of altered mechanical properties in myocardium after hydrogel injection. Ann Biomed Eng. 2013 [Epub ahead of print].

15. Rane, Aa; Chuang, JS.; Shah, A.; Hu, DP.; Dalton, ND.; Gu, Y., et al. Increased infarct wall thickness by a bio-inert material is insufficient to prevent negative left ventricular remodeling after myocardial infarction. PLoS One. 2011; 6:e21571. [PubMed: 21731777]

16. Seif-Naraghi SB, Salvatore MA, Schup-Magoffin PJ, Hu DP, Christman KL. Design and characterization of an injectable pericardial matrix gel: a potentially autologous scaffold for cardiac tissue engineering. Tissue Eng Part A. 2010; 16:2017–2027. [PubMed: 20100033]

17. Christman KL, Vardanian AJ, Fang Q, Sievers RE, Fok HH, Lee RJ. Injectable fibrin scaffold improves cell transplant survival, reduces infarct expansion, and induces neovasculature formation in ischemic myocardium. J Am Coll Cardiol. 2004; 44:654–660. [PubMed: 15358036]

18. Sun Y, Kiani MF, Postlethwaite AE, Weber KT. Infarct scar as living tissue. Basic Res Cardiol. 2002; 97:343–347. [PubMed: 12200633]

19. Rosenzweig A. Cardiac cell therapy--mixed results from mixed cells. N Engl J Med. 2006; 355:1274–1277. [PubMed: 16990391]

20. Weber KT. Fibrosis in hypertensive heart disease : focus on cardiac fibroblasts. J Hypertens. 2004:47–50. [PubMed: 15106793]

21. Camelliti P, Green CR, Kohl P. Structural and functional coupling of cardiac myocytes and fibroblasts. Adv Cardiol. 2006; 42:132–149. [PubMed: 16646588]

22. Bryant JE, Shamhart PE, Luther DJ, Olson ER, Koshy JC, Costic DJ, et al. Cardiac myofibroblast differentiation is attenuated by alpha(3) integrin blockade: potential role in post-MI remodeling. J Mol Cell Cardiol. 2009; 46:186–192. [PubMed: 19041328]

23. Asazuma-Nakamura Y, Dai P, Harada Y, Jiang Y, Hamaoka K, Takamatsu T. Cx43 contributes to TGF-beta signaling to regulate differentiation of cardiac fibroblasts into myofibroblasts. Exp Cell Res. 2009; 315:1190–1199. [PubMed: 19162006]

24. Ayala P, Lopez J, Desai T. Microtopographical cues in 3D attenuate fibrotic phenotype and extracellular matrix deposition: implications for tissue regeneration. Tissue Eng Part A. 2010; 16:2519–2527. [PubMed: 20235832]

25. Ayala P, Desai TA. Integrin α3 blockade enhances microtopographical down-regulation of α-smooth muscle actin: role of microtopography in ECM regulation. Integr Biol (Camb). 2011; 3:733–741. [PubMed: 21666923]

26. Boateng SY, Hartman TJ, Ahluwalia N, Vidula H, Desai Ta, Russell B. Inhibition of fibroblast proliferation in cardiac myocyte cultures by surface microtopography. Am J Physiol Cell Physiol. 2003; 285:C171–C182. [PubMed: 12672651]

27. Norman JJ, Collins JM, Sharma S, Russell B, Desai Ta. Microstructures in 3D biological gels affect cell proliferation. Tissue Eng Part A. 2008; 14:379–390. [PubMed: 18333790]

28. Thakar RG, Chown MG, Patel A, Peng L, Kumar S, Desai Ta. Contractility-dependent modulation of cell proliferation and adhesion by microscale topographical cues. Small. 2008; 4:1416–1424. [PubMed: 18711756]

29. Huang NF, Sievers RE, Park JS, Fang Q, Li S, Lee RJ. A rodent model of myocardial infarction for testing the efficacy of cells and polymers for myocardial reconstruction. Nat Protoc. 2006; 1:1596–1609. [PubMed: 17406452]

30. Yu J, Christman KL, Chin E, Sievers RE, Saeed M, Lee RJ. Restoration of left ventricular geometry and improvement of left ventricular function in a rodent model of chronic ischemic cardiomyopathy. J Thorac Cardiovasc Surg. 2009; 137:180–187. [PubMed: 19154923]

31. Leask A. Potential therapeutic targets for cardiac fibrosis: TGFbeta, angiotensin, endothelin, CCN2, and PDGF, partners in fibroblast activation. Circ Res. 2010; 106:1675–1680. [PubMed: 20538689]

32. Akhmetshina A, Palumbo K, Dees C, Bergmann C, Venalis P, Zerr P, et al. Activation of canonical Wnt signalling is required for TGF-β-mediated fibrosis. Nat Commun. 2012; 3:735. [PubMed: 22415826]

33. Yang Y, Zhe X, Phan SH, Ullenbruch M, Schuger L. Involvement of serum response factor isoforms in myofibroblast differentiation during bleomycin-induced lung injury. Am J Respir Cell Mol Biol. 2003; 29:583–590. [PubMed: 12777247]

34. Mendez MG, Janmey PA. Transcription factor regulation by mechanical stress. Int J Biochem Cell Biol. 2012; 44:728–732. [PubMed: 22387568]

35. Khan R, Sheppard R. Fibrosis in heart disease: understanding the role of transforming growth factor-beta in cardiomyopathy, valvular disease and arrhythmia. Immunology. 2006; 118:10–24. [PubMed: 16630019]

36. Dupont S, Morsut L, Aragona M, Enzo E, Giulitti S, Cordenonsi M, et al. Role of YAP/TAZ in mechanotransduction. Nature. 2011; 474:179–183. [PubMed: 21654799]

37. Swift J, Ivanovska IL, Buxboim A, Harada T, Dingal PCDP, Pinter J, et al. Nuclear lamin-A scales with tissue stiffness and enhances matrix-directed differentiation. Science. 2013; 341:1240104. [PubMed: 23990565]

38. Bainer R, Weaver V. Cell biology. Strength under tension. Science. 2013; 341:965–966. [PubMed: 23990548]

39. Sun Y, Zhang JQ, Zhang J, Lamparter S. Cardiac remodeling by fibrous tissue after infarction in rats. J Lab Clin Med. 2000; 135:316–323. [PubMed: 10779047]

40. Stanton LW, Garrard LJ, Damm D, Garrick BL, Lam a, Kapoun aM, et al. Altered patterns of gene expression in response to myocardial infarction. Circ Res. 2000; 86:939–945. [PubMed: 10807865]

41. Rehfeldt F, Engler AJ, Eckhardt A, Ahmed F, Discher DE. Cell responses to the mechanochemical microenvironment--implications for regenerative medicine and drug delivery. Adv Drug Deliv Rev. 2007; 59:1329–1339. [PubMed: 17900747]

42. Patel, Aa; Thakar, RG.; Chown, M.; Ayala, P.; Desai, Ta; Kumar, S. Biophysical mechanisms of single-cell interactions with microtopographical cues. Biomed Microdevices. 2010; 12:287–296. [PubMed: 20033299]

43. Gould ST, Anseth KS. Role of cell-matrix interactions on VIC phenotype and tissue deposition in 3D PEG hydrogels. J Tissue Eng Regen Med. 2013 [Epub ahead of print].

44. Kirschner CM, Anseth KS. Hydrogels in healthcare: From static to dynamic material microenvironments. Acta Mater. 2013; 61:931–944. [PubMed: 23929381]

45. Tibbitt MW, Kloxin AM, Sawicki LA, Anseth KS. Mechanical properties and degradation of chain and step-polymerized photodegradable hydrogels. Macromolecules. 2013; 46:2785–2792.
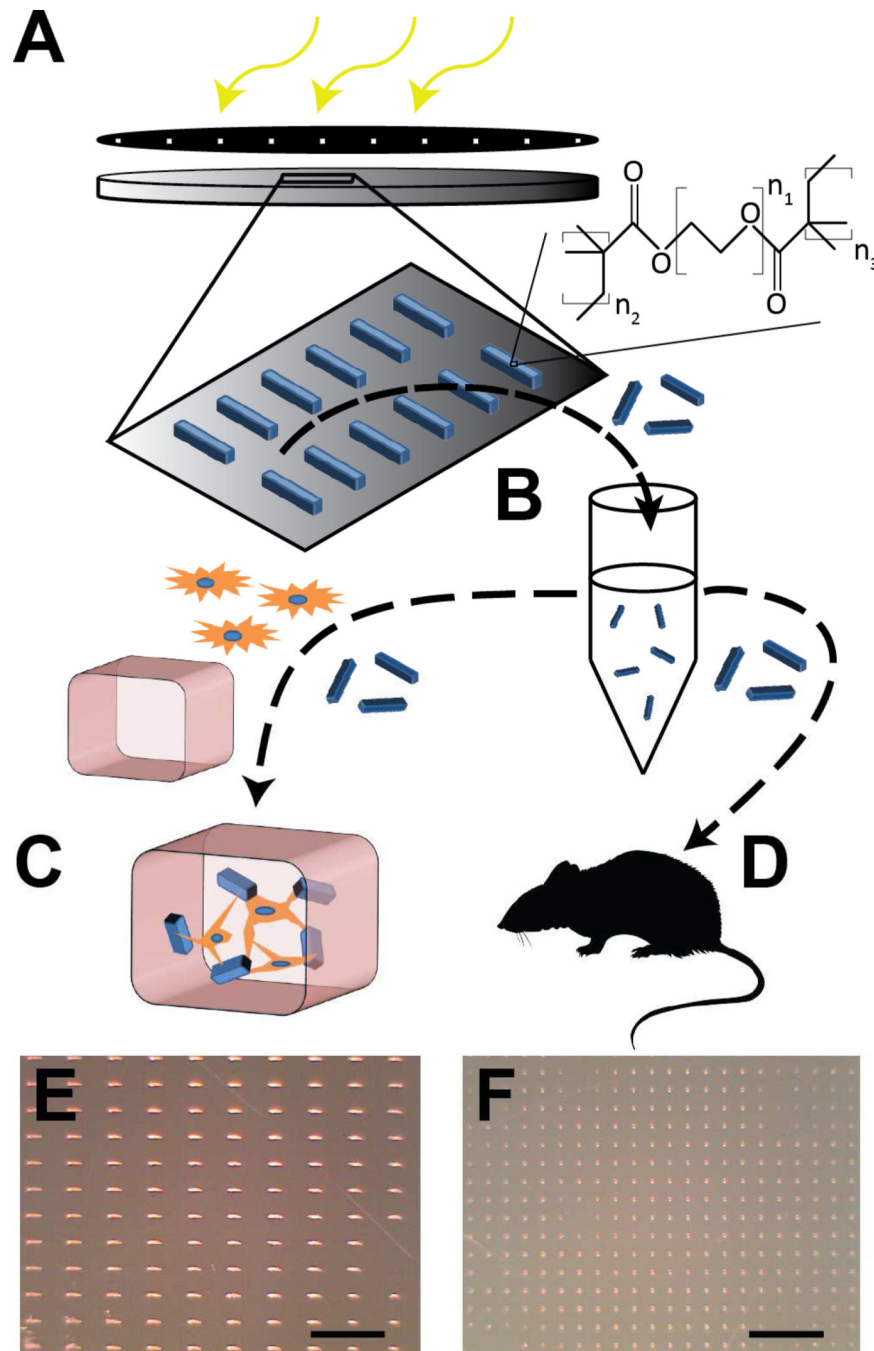
Fig. 1. Microstructure fabrication and experiment design
Microstructures are fabricated photolithographically by exposure of a thin film of hydrogel polymer to UV energy through a patterned photomask **(A)**. Microrods and microcubes are released from the surface in sterile saline solution **(B)**. From here, the microstructures are either added to a solution of fibroblasts and liquid phase Matrigel to create *in vitro* 3D tissue constructs for study of cell-microstructure interactions **(C)**, or are injected in saline solution into the infarct zone of Sprague-Dawley rats under ultrasound guidance 48 hours after

temporary LAD ligation and reperfusion **(D)**. Light micrographs show high throughput arrays of microrods **(E)** and microcubes **(F)** on a silicon wafer. Scale bar = 500 μm.
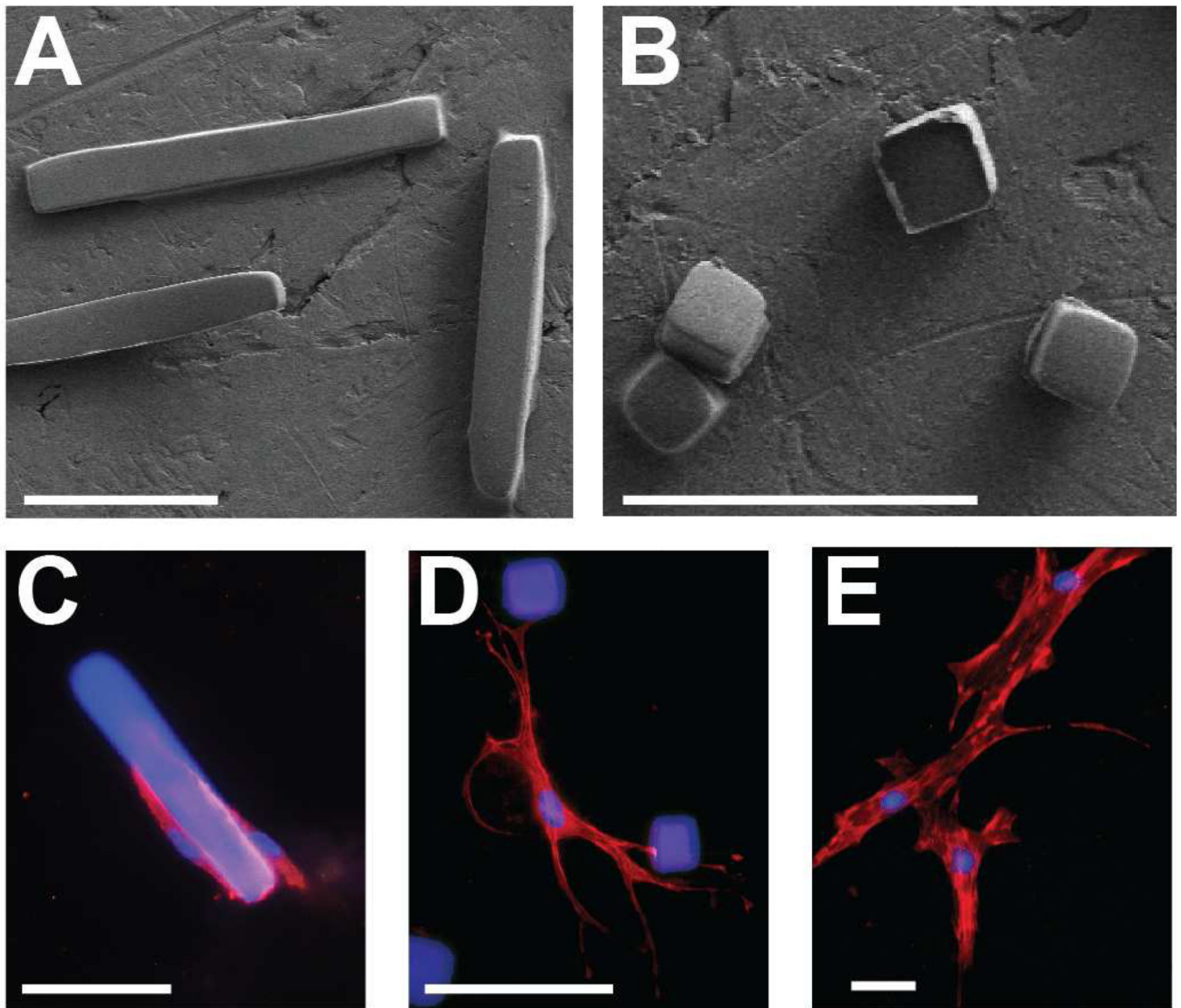
Fig. 2. Microrods and microcubes interact with fibroblasts *in vitro*
Scanning electron micrograph of free-standing microstructures fabricated from polymerized polyethylene glycol dimethacrylate ("microrods", 100 μm × 15 μm × 15 μm (**A**); "microcubes", 15 μm × 15 μm × 15 μm (**B**)). Fluorescent immunocytochemical stain of adult Sprague-Dawley ventricular cardiac fibroblasts interacting with a microrod (**C**), microcubes (**D**), or in the absence of microstructures (**E**) suspended in a 3D culture of Matrigel. Scale bar = 50 μm (red = rhodamine phalloidin, blue = nuclei and microstructures).
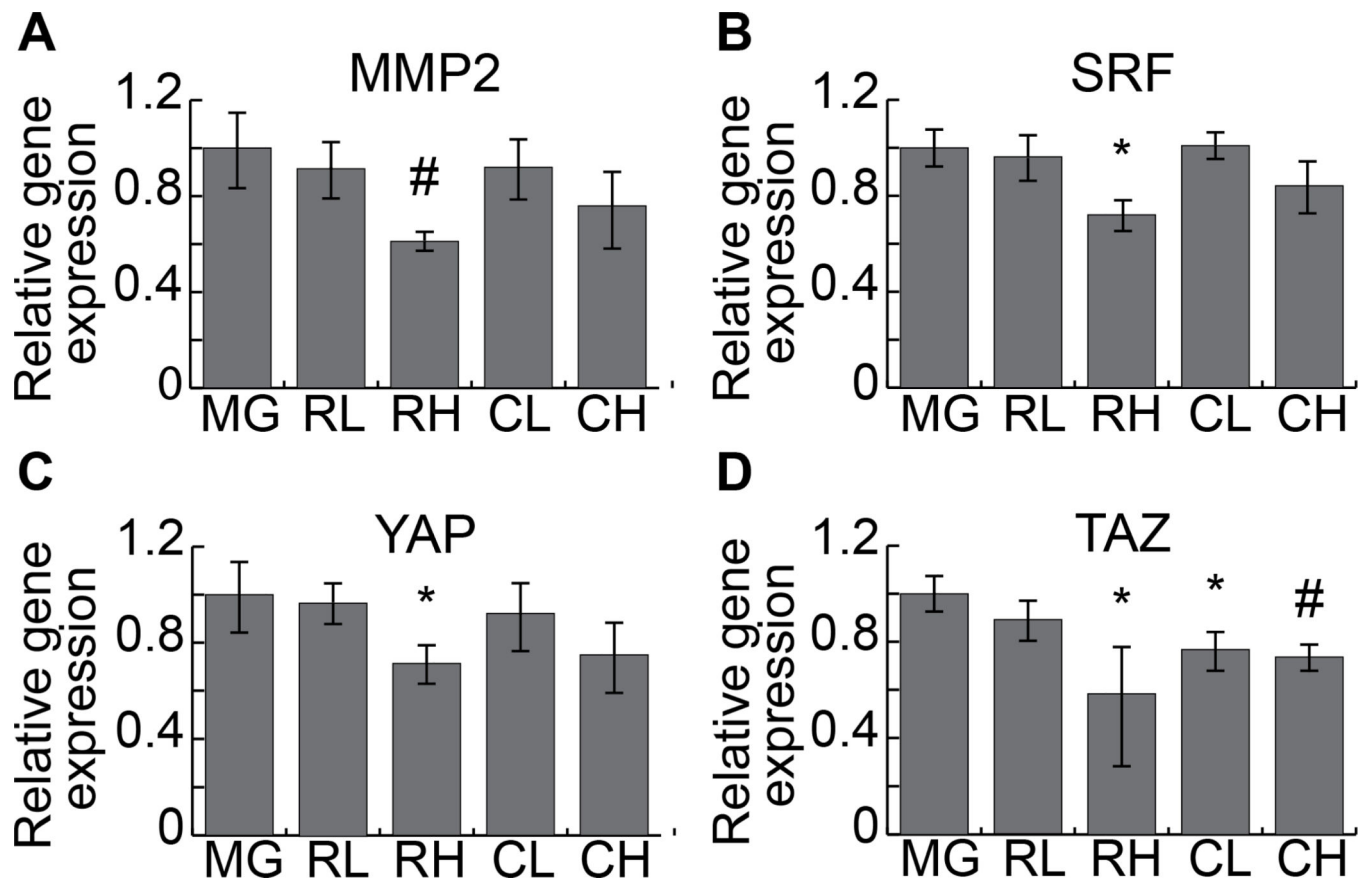
Fig. 3. Gene expression analysis of microrods and microcubes in 3D cell culture
Fibroblasts cultured in three-dimensional constructs in the presence of varying concentrations of microrods and microcubes show a decrease in the expression of mmp2 (**A**), SRF (**B**), YAP1 (**C**), and TAZ (**D**), in a dose dependent manner for both structure types, as compared to gel constructs with no microstructures (n = 3). (Two-tailed student's t-test, * = $p < 0.05$, # = $p < 0.01$, as compared to Matrigel only. Data points indicate the mean of three biological replicates each composed of a pooled sample from multiple cultures. Error bars = 95% confidence intervals.) (MG = Matrigel alone; RL = microrods, low concentration; RH = microrods, high concentration; CL = microcubes, low concentration; CH = microcubes, high concentration).
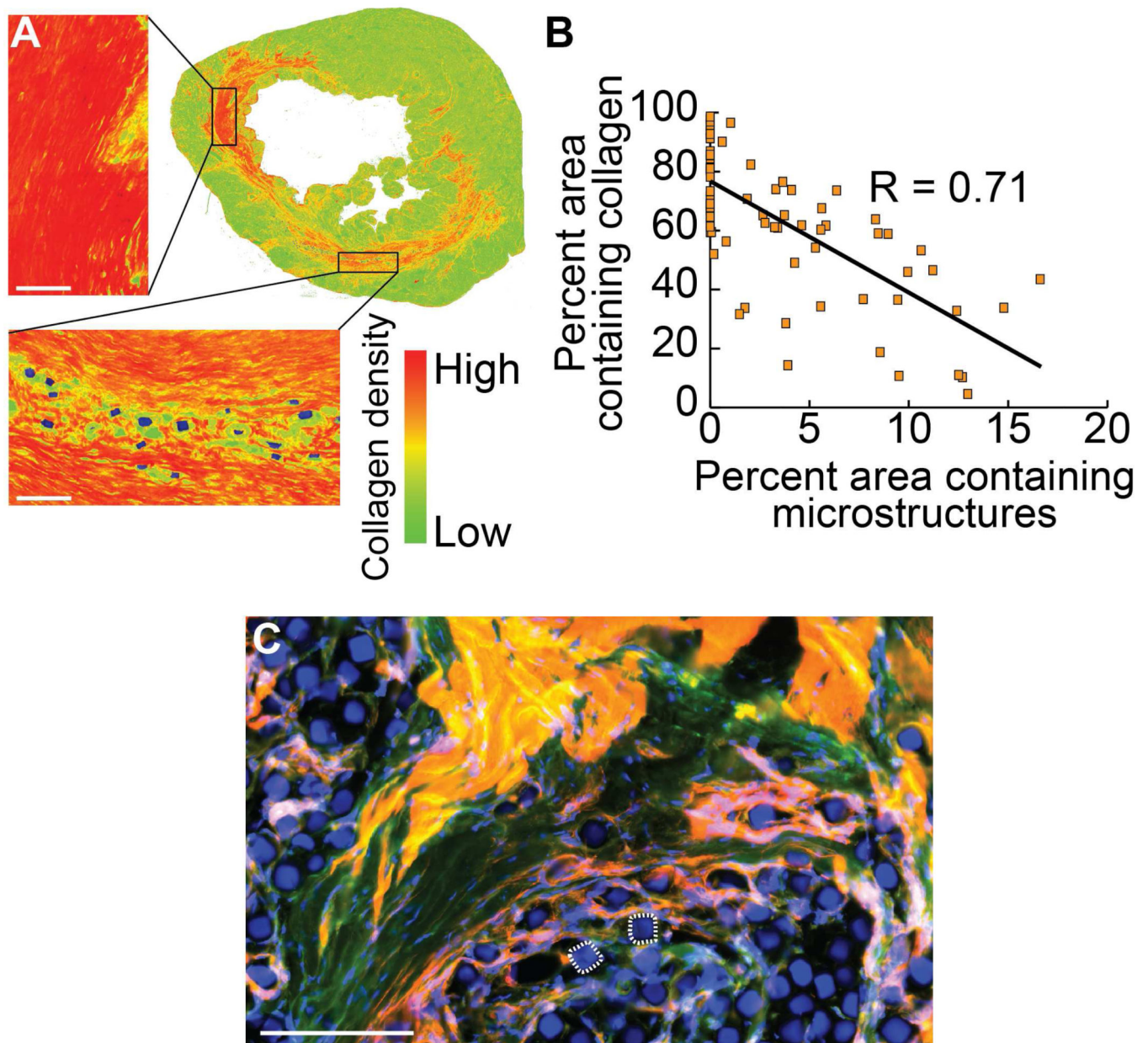
Fig. 4. Collagen production reduced proximal to microstructures *in vivo*
Local changes in the makeup of the scar tissue are seen in the presence of microstructures. A representative aniline blue stained left ventricle of an infarcted rat treated with a single injection of microcubes is false-colored to depict collagen density based on colorimetric stain intensity (**A**), showing an inverse relationship between local collagen content and coverage area by microstructures after six weeks in the scarred region surrounding the injection site (Pearson Correlation Coefficient: R = 0.71) (**B**). Microstructures make independent and intimate contact with surrounding fibrotic and healthy cardiac tissue at the cellular level, analogous to the interactivity seen in the *in vitro* culture model. Two microcubes are outlined for reference (**C**). Scale bar = 100 μm (red = rhodamine phalloidin, green = myosin heavy chain antibody, blue = nuclei and microstructures).
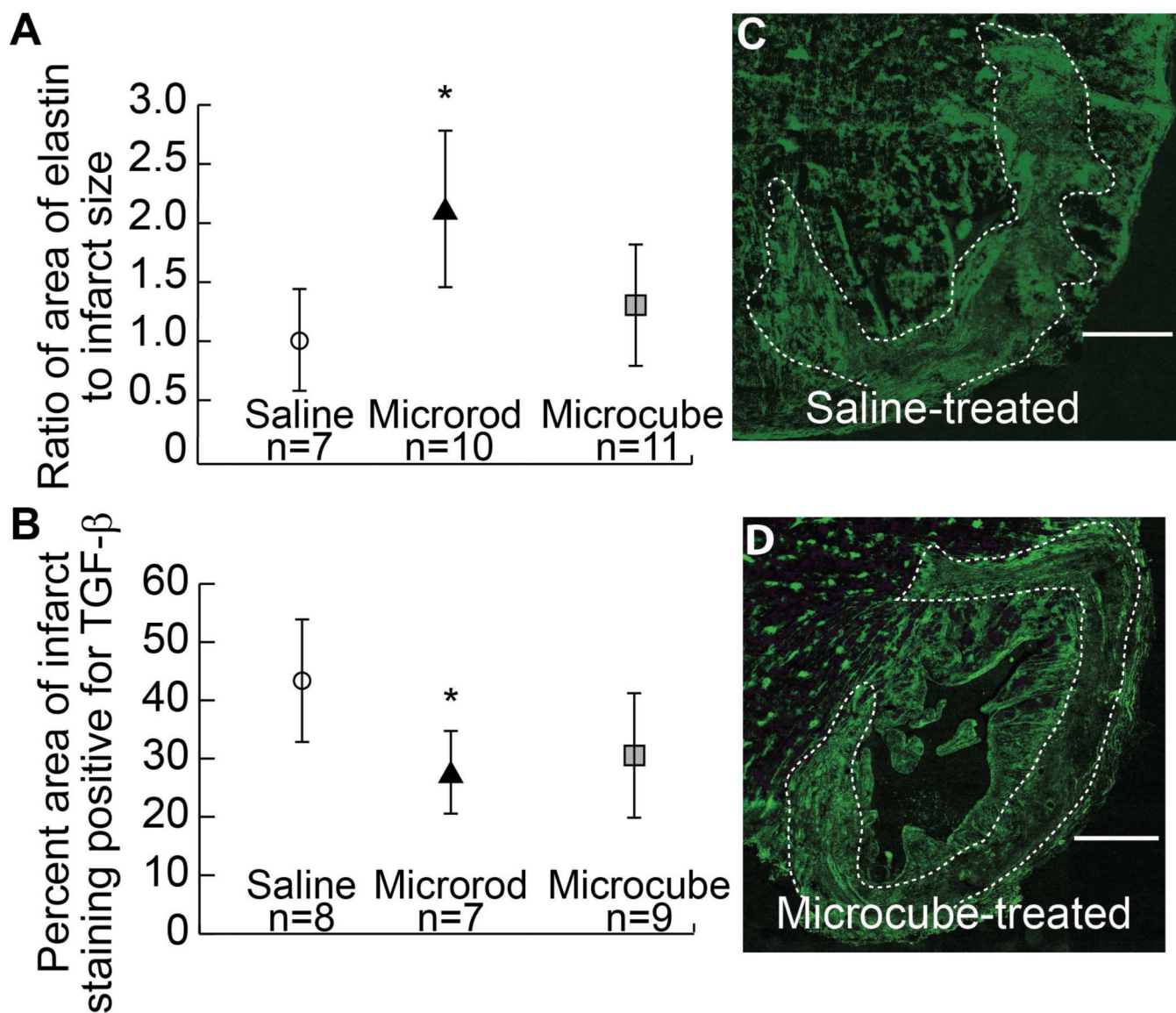
Fig. 5. Elastin and TGF-β expression altered by microstructures in the infarct zone

Quantification of the relative coverage area of elastin staining in the infarct zone as normalized to that seen in saline-treated animals shows a significant two-fold increase in elastin content in microrod treated hearts (p = 0.01 by student's t-test, p = 0.05 by Mann-Whitney test) and a mild increase in microcube-treated hearts (p = 0.2 by student's t-test, p = 0.4 by Mann-Whitney test) **(A)**. Quantification of the percentage of the infarct zone staining positive for TGF-β shows a significant decrease in expression in microrod-treated hearts (p = 0.02) and a trend toward decreased expression in microcube-treated hearts (p = 0.05) **(B)**. Fluorescent immunohistochemistry for TGF-β in the infarct region shows high staining density in saline-treated hearts **(C)** and reduced TGF-β content in microcube-treated hearts **(D)**. White dotted outline indicates infarct. Scale bar = 1 mm (One-tailed student's t-test and Mann-Whitney test as alternative consideration in cases of potential asymmetric data

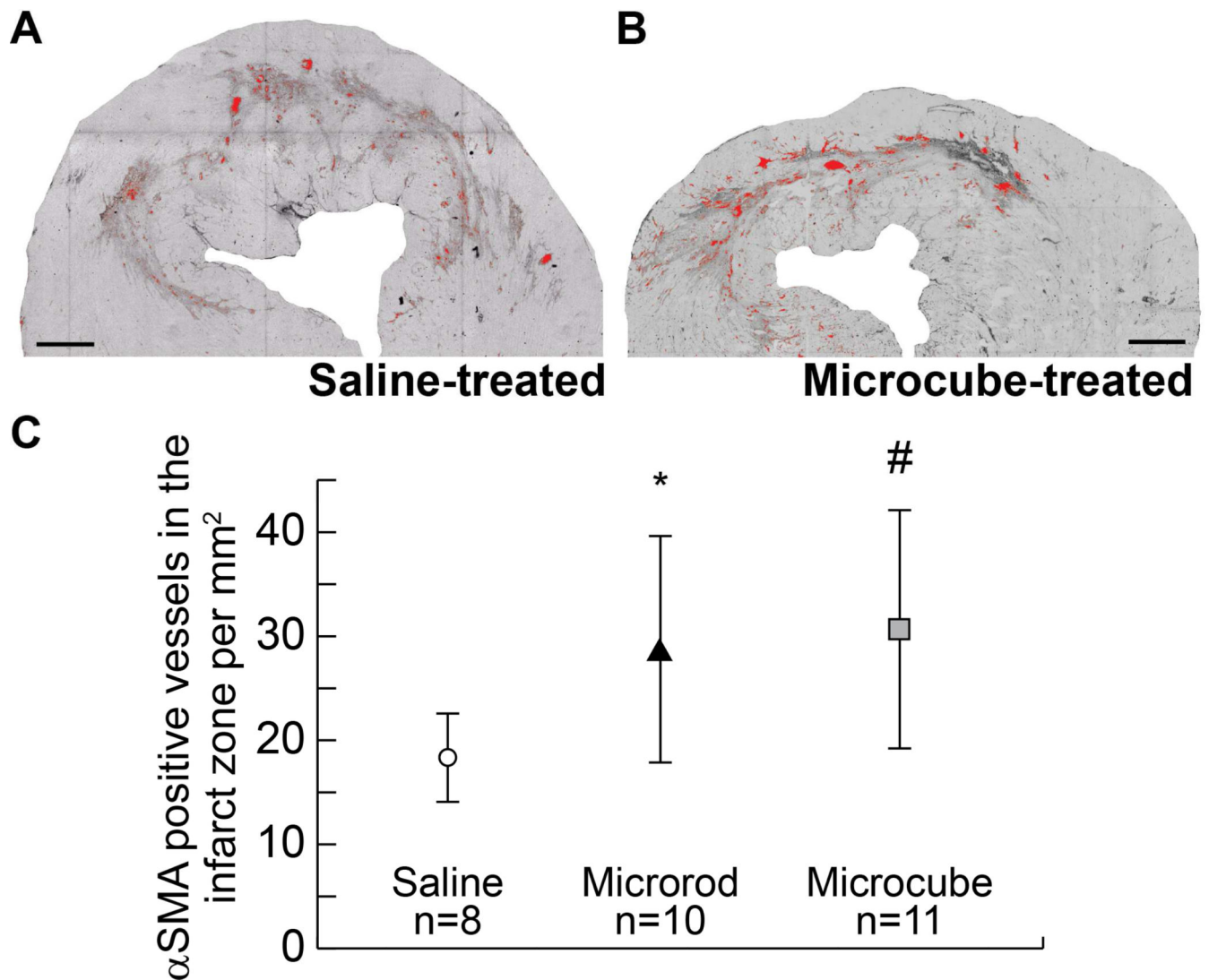distribution, * = p < 0.05 by student's t-test. Data points indicate the mean. Error bars = 95% confidence intervals).

Fig. 6. Enhanced vascularization in the infarct zone after treatment
Representative image of a saline-treated **(A)** and microcube-treated **(B)** infarct immunohistochemically stained for αSMA. Vessels were counted and normalized to the area of the infarct and highlighted in red for visualization. Quantification of the number of αSMA-positive vessels per infarct area shows a significant increase in the density of vessels in microrod-treated hearts (p = 0.01 by student's t-test, p = 0.005 by Mann-Whitney test) and microcube-treated hearts (p = 0.005 by student's t-test, p = 0.002 by Mann-Whitney test) **(C)**. Scale bar = 1 mm (One-tailed student's t-test and Mann-Whitney test as alternative consideration in cases of potential asymmetric data distribution, * = p < 0.05, # = p < 0.01 as compared to saline control by student's t-test. Data points indicate the mean. Error bars = 95% confidence intervals).
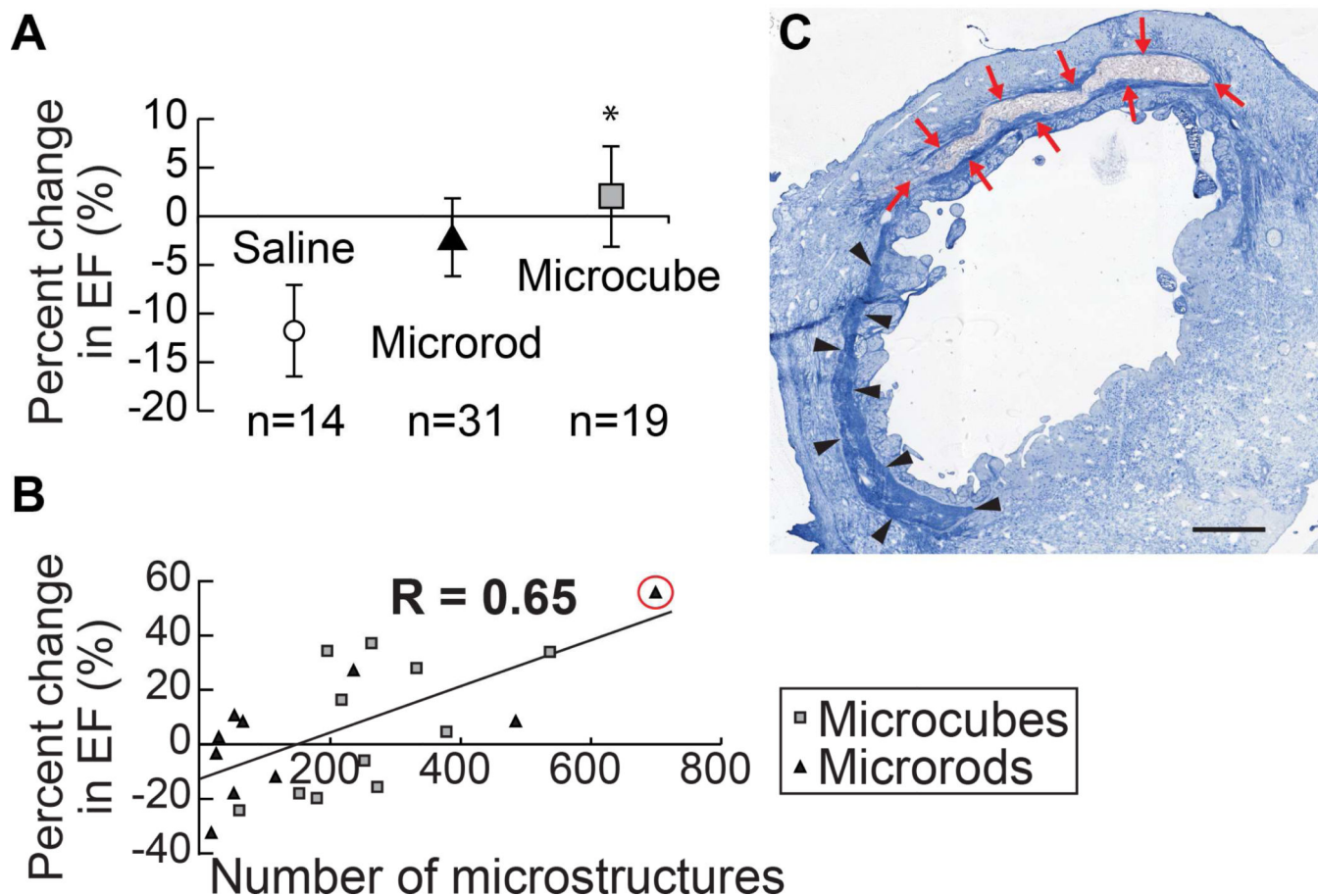
Fig. 7. Functional benefits of microstructure injection

The relative change in ejection fraction (EF) over the course of the six weeks as compared to the EF after infarct induction, immediately preceding microstructure injection or saline control injection, was calculated by the formula $(EF_{6\ weeks} - EF_{initial})/EF_{initial}$. Injection of microrods and microcubes mitigated the chronic decline in heart function typically seen in untreated hearts, as depicted by the saline-injected control group. (One-tailed student's t-test, * = $p < 0.05$ as compared to saline control. Data points indicate the mean. Error bars represent 95% confidence intervals) **(A)**. Microstructures recovered in the tissue were quantified, showing a direct correlation between functional outcomes and microstructure delivery efficiency (Pearson Correlation Coefficient, R = 0.65) **(B)**. Aniline blue stained section of the highest performing heart (change in EF = +56%) shows a large pocket of microrods in the infarct zone with reduced adjacent collagenous scarring (arrows, red) as compared to the distal region of the infarct with no microrods present (arrowheads, black) **(C)**. Scale bar = 1 mm.